Structural, mechanical and Raman spectroscopic characterization of the layered uranyl silicate mineral, uranophane-α, by density functional theory methods

FRANCISCO COLMENERO [1],*, VICENTE TIMÓN [1],
LAURA J. BONALES [2] AND JOAQUÍN COBOS [2]

[1] *Instituto de Estructura de la Materia, CSIC, C/Serrano, 113, 28006 Madrid, Spain*
[2] *Centro de Investigaciones Energéticas, Medioambientales y Tecnológicas, CIEMAT, Avda/Complutense, 40, 28040 Madrid, Spain*

ABSTRACT: The layered uranyl silicate clay-like mineral, uranophane-α, $Ca(UO_2)_2(SiO_3OH)_2\cdot 5H_2O$, was studied by first-principles calculations based on the density functional theory method. The structure, observed in nature in a wide variety of compounds having the uranophane sheet anion topology, is confirmed here for the first time by means of rigorous theoretical solid-state calculations. The computed lattice parameters, bond lengths and bond angles were in very good agreement with the experimental ones, and the calculated X-ray powder trace accurately reproduced its experimental counterpart. The mechanical properties of uranophane-α, for which there are no experimental data for terms of comparison, were determined, and the satisfaction of the mechanical stability Born conditions of the structure was demonstrated by calculations of the elasticity tensor. The Raman spectrum was computed by the density functional perturbation theory and compared with the experimental spectrum. The vibrational properties of this mineral were well characterized, showing a good performance in all of the studied spectral range. Theoretical methods allowed assignment of the Raman bands to vibrations localized in different fragments within the crystal unit cell. Finally, the possibility of incorporation of strontium inside the uranophane structure was studied. The computed structure, X-ray powder trace and Raman spectrum of Sr-exchanged uranophane were very close to those of the ordinary Ca-uranophane.

KEYWORDS: spent nuclear fuel, uranophane-α, DFT calculations, uranyl silicate minerals, Raman spectroscopy, cation exchange.

Uranyl silicates form as alteration products during hydration–oxidation weathering of uraninite (Frondel, 1956; Finch & Ewing, 1992) and from spent nuclear fuel (SNF) (Wronkiewicz *et al.*, 1992, 1996; Pearcy *et al.*, 1994; Plasil, 2014), which is mainly composed of uranium dioxide (UO_2). The contact between groundwaters containing dissolved silicate and dissolved uranyl is expected to produce uranyl silicate minerals (Wronkiewicz *et al.*, 1992, 1996; Pearcy *et al.*, 1994; Plasil, 2014). These minerals play a major role in the long-term dosage of nuclear waste repositories. The ubiquity of uranophane-α suggests

that the uranyl silicates are among the most important phases controlling uranium concentrations in groundwater (Finch & Ewing, 1992; Plasil, 2014).

Mineral uranophane-α, a hydrated uranyl nesosilicate, $Ca(UO_2)_2(SiO_3OH)_2 \cdot 5H_2O$, was one of the earliest known uranyl minerals, which was first described by Websky (1853, 1859). Since then, it has been identified in nearly all major and most of the minor uranium deposits in the world. Its β-polymorph, also monoclinic (Viswanathan & Harneit, 1986; Burns, 1999a), is much rarer and was observed for the first time by Novacek (1935).

Uranophane-α is characterized by a 1:1 uranium to silicon ratio (Stohl & Smith, 1981). Its structure is very complex and includes 68 atoms in the unit cell, as well as 320 valence electrons. Uranyl silicate minerals having this ratio contain sheets (Stohl & Smith, 1981; Burns, 2005; Grenthe et al., 2006). Nine uranyl silicate minerals (uranophane-α and -β, sklodowskite, cuprosklodowskite, boltwoodite, sodium boltwoodite, kasolite, oursinite and swamboite) have been classified as members of the uranophane group on the basis of the uranium to silicon ratio and their similar uranophane anion sheet topology (Burns et al., 1996, 1997a; Burns, 1998, 1999a, 2005; Grenthe et al., 2006).

Uranyl silicate minerals behave much like clay minerals. They form layers composed of sheets having a net negative charge that stack up with cations in the interlayer space to provide charge balance within the structure (Burns, 1999b, 2005; Burns & Li, 2002; Douglas et al., 2002; Grenthe et al., 2006). Uranyl cations in the sheet might be replaced by other non-uranyl cations, similar to cation substitution in the sheets of clay minerals, providing a mechanism for incorporation of transuranic elements into these phases (Burns et al., 1996, 1997a,b, 2004; Burns, 1998; Douglas et al., 2005; Murphy & Grambow, 2008; Burns & Klingensmith, 2006; Klingensmith & Burns, 2007; Shuller et al., 2010, 2013, 2014; Kuta et al., 2013). Other cations may be substituted into the interlayer space via ion exchange, providing a mechanism of incorporation of fission products such as caesium or strontium (Burns et al., 1996, 1997a; Burns, 1998, 1999b, 2005; Burns & Li, 2002; Douglas et al., 2002). Thus, these mineral phases formed at the SNF surface may potentially act as an additional barrier to radionuclide migration via mineral sorption reactions. The incorporation mechanisms seem to be more favourable in structures with charged sheets and cations in the interlayer than in structures with electroneutral sheets, since coupled substitutions involving the interlayer may represent a charge-balancing mechanism that permits the substitution (Burns & Klingensmith, 2006; Klingensmith & Burns, 2007).

While the structure of uranophane has been determined by experimental X-ray diffraction (XRD) techniques (Ginderow, 1988), it has never been confirmed by means of theoretical solid-state calculations. Although classical molecular dynamics methods based in empirical force fields have been employed to study the uranophane–water interface, as well as the interfacial reactivity of this uranyl silicate (Kuta et al., 2013), rigorous first-principles methods have only been used by Kuta et al. (2013) and Wheaton et al. (2003) to study uranyl silicate clusters.

To the authors' knowledge, no experimental or computational studies have been reported regarding the mechanical properties of uranophane, and the conditions of mechanical stability of its structure have not been investigated. The confirmation of the structure and stability of the uranophane structure by means of first-principles methods is also relevant because this structure represents one of the most fundamental anion topologies in the U(VI) minerals, referred to as the 'uranophane sheet anion topology' in the literature (Burns et al., 1996, 1997a; Burns, 1998, 1999a, 2005; Grenthe et al., 2006). This topology is also the basis of the structure of a large series of phosphates, arsenates, vanadates and molybdates (Forbes & Burns, 2006; Grenthe et al., 2006; Jouffret et al., 2010a,b,c; Jin et al., 2011; Mer et al., 2012).

The radiotoxicity of these substances complicates their handling under security conditions and, therefore, their characterization. The most appropriate characterization techniques for analysing these materials should be non-destructive, should not require any special sample preparation and should allow the analysis of very small amounts of sample. A technique satisfying these requirements is Raman spectroscopy. Raman spectra of uranyl silicate minerals have been given by Frost et al. (2006a,b), Amme et al. (2002), Bonales et al. (2015) and Driscoll et al. (2014). A very complete characterization study of uranophane including scanning electron microscopy (SEM), XRD, thermogravimetric analysis, surface area and charge determination and Raman spectroscopy was carried out by Wall et al. (2010). Although the Raman spectrum of uranophane has been determined experimentally, a precise assignment of the main bands in the spectrum is lacking. Theoretical methods allow for a complete characterization of these materials free of all the problems associated with its radiotoxicity. The assignment of the experimental vibrational bands is possible as these

methods provide detailed views at a microscopic scale of the atomic vibrational motions in the corresponding normal modes.

METHODS: THEORETICAL DENSITY FUNCTIONAL THEORY (DFT) CALCULATIONS

The *CASTEP* code (Clark *et al.*, 2005), a module of the Materials Studio package (Materials Studio, 2018), was employed to model the uranophane-α structure as in our recent work (Bonales *et al.*, 2016; Colmenero *et al.*, 2017a,b,c,d, 2018a,b). Also, the generalized gradient approximation (GGA) together with the Perdew–Burke–Ernzerhof (PBE) functional (Perdew *et al.*, 1996) and Grimme empirical dispersion correction – the DFT-D2 approach (Grimme *et al.*, 2006) – were employed. The introduction of dispersion corrections produces a remarkable improvement in the results for systems in which the accurate description of non-bonded interactions is important (Tunega *et al.*, 2012). A norm conserving relativistic pseudopotential (Troullier & Martins, 1991) for the uranium atom, generated in a previous work (Bonales *et al.*, 2016), was used here. This pseudopotential was employed for other theoretical studies of uranyl-containing materials, such as rutherfordine (Bonales *et al.*, 2016; Colmenero *et al.*, 2017a), studtite (Colmenero *et al.*, 2017b), soddyite (Colmenero *et al.*, 2017c) and γ-UO_3 polymorph (Colmenero *et al.*, 2017d).

The methods employed for geometry optimization and calculation of vibrational Raman spectra, mechanical properties and equations of state (EOSs) were the same as in previous studies (Bonales *et al.*, 2016; Colmenero *et al.*, 2017a,b,c,d), and their description will be not repeated here. However, present uranophane computations required larger kinetic energy cutoffs and K-point meshes to ensure good convergence for computed structures and energies. A kinetic energy cut-off of 1000 eV and a K mesh of $3 \times 3 \times 1$ (four K points) were selected to determine the final results.

RESULTS AND DISCUSSION

Uranophane structure

The unit cell of uranophane-α, $Ca(UO_2)_2$ $(SiO_3OH)_2 \cdot 5H_2O$, has monoclinic symmetry, space group $P2_1$ ($Z = 4$). It contains 68 atoms: 4 U, 4 Si, 2 Ca, 34 O and 24 H. In our computations, 320 valence electrons were described explicitly.

Stohl and Smith (1981) categorized naturally occurring uranyl silicates according to the uranium to silicon ratio, which in part determines the structures of these minerals. Most uranyl silicate minerals have 1:1 uranium to silicon ratios and are sheet silicates (Stohl & Smith, 1981; Burns, 2005; Grenthe *et al.*, 2006). Soddyite has a 2:1 uranium to silicon ratio and a framework crystal structure (Stohl & Smith, 1981; Demartin *et al.*, 1992; Burns, 2005). The ratio of 2:5 was found in the crystal structures of weeksite (Jackson & Burns, 2001), haiweeite (Burns, 2001) and coutinhoite (Atencio *et al.*, 2004), and probably also in some uranyl silicate minerals from Russia that have not been approved by the International Mineralogical Association. Some synthetic framework uranyl silicates have also been described (Burns & Hill, 2000; Huang *et al.*, 2003).

Uranyl silicate sheets are composed of $[(UO_2)_2 (SiO_4)_2]^{-4}$ units bound at the equatorial edges (see Fig. 1a,b). A sheet, $[(UO_2)(SiO_4)]_n^{-2n}$, contains UO_7 pentagonal bipyramids and SiO_3OH tetrahedra. Charge-compensating cations – calcium in uranophane – lie in the interlayer space between the sheets (see Fig. 1c). Two uranyl silicate sheets are connected by $CaO_2(OH)(H_2O)_4$ polyhedra (distorted pentagonal bipyramid). The Ca atom ligands are four water molecules, two uranyl oxygen atoms belonging to the upper and the lower sheets and one OH group of a SiO_3OH tetrahedron. One water molecule is out of the Ca polyhedron. While this water molecule is described as free or as crystallization water, the four water molecules belonging to the Ca atom coordination sphere are referred to as structural water. Hydrogen bonds reinforce the bonding between the uranyl silicate sheets, the Ca atom and the free water. The upper sheet SiO_3OH tetrahedra have free OH groups pointing downwards and the lower sheet tetrahedra have OH groups pointing upwards, which belong to the Ca atom coordination sphere (Fig. 1c).

The structure of uranophane-α was determined in calculations with increasing complexity in order to obtain a set of calculation parameters yielding good convergence for computed structures and energies. Table 1 gives the final lattice parameters, volumes and densities obtained compared with the corresponding experimental values of Ginderow (1988). The agreement is excellent, with the error in the computed volume and density being only ~0.4%.

Table 2 shows a comparison of the more important geometric parameters (bond distances) obtained with the corresponding experimental data of Ginderow (1988). Uranophane-α has two structurally
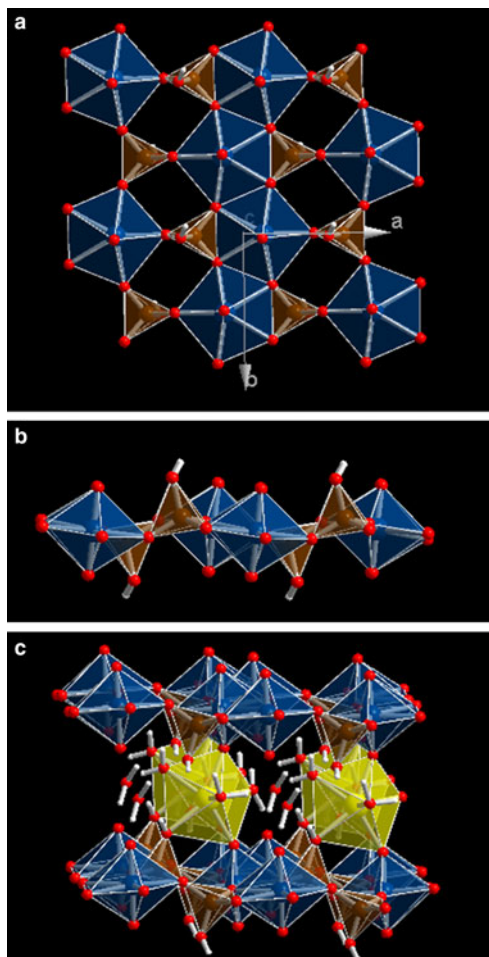
FIG. 1. Structure of uranophane-α. (a) View of a $2 \times 2 \times 2$ supercell from [001] showing a uranyl silicate sheet $[(UO_2)(SiO_4)]_n^{-2n}$ composed of UO_7 pentagonal bipyramids and SiO_3OH tetrahedral. (b) The same view as in (a) from [010]. (c) View of a $2 \times 2 \times 2$ supercell from [010] showing two uranyl silicate sheets connected by $CaO_2(OH)(H_2O)_4$ polyhedra (distorted pentagonal bipyramid). One water molecule is out of the Ca polyhedron (free water). Colour code: U = blue; Si = brown; O = red; H = white; Ca = yellow.

(symmetrically) identical U^{6+} ions and two structurally (symmetrically) identical Si^{4+} ions in its crystal structure. However, the two non-symmetrically related uranyl and silicate polyhedra are nearly identical. The two O atoms in the uranyl group, UO_2^{2+}, are in apical positions of the pentagonal bipyramids at distances of 1.801 and 1808 Å for both U1 and U2. The calculated values are 1.828 and

1.843 Å for U1 and 1.825 and 1.829 Å for U2, respectively. The remaining five O atoms lie in the equatorial plane, with the U–O distances ranging from 2.241 to 2.463 Å (calculated 2.214–2.457 Å for U1 and 2.236–2.462 Å for U2, respectively). The Si–O distances, ranging from 1.601 to 1.638 Å, are within the normal range (calculated 1.621–1.663 Å for Si1 and 1.620–1.666 Å for Si2, respectively). Ca–O distances in the distorted pentagonal bipyramid are satisfactorily reproduced and range from 2.371 to 2.445 Å (calculated 2.372–2.509 Å). Thus, the solvation structure around the interlayer Ca atom is described satisfactorily.

It is concluded that the experimental geometrical parameters and our theoretical values agree quite well in spite of the complexity of the uranophane-α structure.

The X-ray powder pattern of uranophane-α was computed from the experimental (Ginderow, 1988) and computed structures (Downs, 1993). The most intense lines (I >10%) are compared in Supplementary Figs S1b and S1c, respectively, and the agreement in line positions and intensities is very good. The precise values of the main reflections are given in Supplementary Table S1.

Mechanical properties and stability

The elastic tensor, needed for the calculation of mechanical properties and to study the mechanical stability of the uranophane crystal structure, was calculated for the optimized equilibrium structure from stress–strain relations by using the finite deformation technique implemented in *CASTEP*. Crystals with monoclinic symmetry have 13 non-degenerate elastic constants in the symmetric stiffness matrix (Nye, 1985; Weck *et al.*, 2015), which may be written as:

$$C = \begin{pmatrix} C11 & C12 & C13 & 0 & C15 & 0 \\ C12 & C22 & C23 & 0 & C25 & 0 \\ C13 & C23 & C33 & 0 & C35 & 0 \\ 0 & 0 & 0 & C44 & 0 & C46 \\ C15 & C25 & C35 & 0 & C55 & 0 \\ 0 & 0 & 0 & C46 & 0 & C66 \end{pmatrix}$$

Here, we use the standard Voigt notation for the indices, contracting a pair of Cartesian indices into a single integer $1 \leq i \leq 6$: xx → 1, yy → 2, zz → 3, yz → 4, xz → 5, xy → 6. The precise values of these constants obtained in our computations are (all values

TABLE 1. Lattice parameters. Experimental values are from Ginderow (1988).

Parameter	a (Å)	b (Å)	c (Å)	α	β	γ	Volume (Å^3)	Density (g/cm^3)
Calculated	6.6689	7.0022	15.8684	90.0	98.0748	90.0	733.6520	3.8766
Experimental	6.665	7.002	15.909	90.0	97.27	90.0	736.478	3.8618

TABLE 2. Bond distances (in Å). Experimental values are from Ginderow (1988).

Bond	Experimental	Calculated	Bond	Experimental	Calculated
	U1 pentagonal bipyramid			U2 pentagonal bipyramid	
U1-O3	U2-O4	1.801	U2-O4	1.801	1.825
U1-O1	U2-O2	1.808	U2-O2	1.808	1.829
U1-O9	U2-O10	2.241	U2-O10	2.241	2.236
U1-O7	U2-O8	2.294	U2-O8	2.294	2.296
U1-O5	U2-O6	2.296	U2-O6	2.296	2.276
U1-O7'	U2-O8'	2.437	U2-O8'	2.437	2.441
U1-O5'	U2-O6'	2.463	U2-O6'	2.463	2.462
Average	Average	2.346	Average	2.346	2.342
	Tetrahedron around Si1			Tetrahedron around Si2	
Si1-O9	1.601	1.621	Si2-O10	1.601	1.620
Si1-O7	1.617	1.644	Si2-O6	1.617	1.639
Si1-O5	1.626	1.642	Si2-O8	1.626	1.643
Si1-O11	1.638	1.663	Si2-O12	1.638	1.666
Average	1.621	1.642	Average	1.621	1.642
		Ca pentagonal bipyramid			
Ca-OW1	2.371	2.372	Ca-O11	2.429	2.420
Ca-OW2	2.387	2.509	Ca-O2	2.432	2.382
Ca-OW3	2.387	2.446	Ca-OW4	2.445	2.474
Ca-O3	2.396	2.387	Average	2.407	2.427

given in GPa):

$$C = \begin{pmatrix} 156.59 & 44.77 & 17.85 & 0 & -6.84 & 0 \\ 44.77 & 152.19 & 14.46 & 0 & 0.60 & 0 \\ 17.85 & 14.46 & 94.34 & 0 & 2.46 & 0 \\ 0 & 0 & 0 & 23.93 & 0 & 2.27 \\ -6.84 & 0.60 & 2.46 & 0 & 27.71 & 0 \\ 0 & 0 & 0 & 2.27 & 0 & 34.54 \end{pmatrix}$$

For monoclinic crystals, a set of necessary (but not sufficient) Born criteria for mechanical stability were given in terms of the stiffness matrix elements, such as by Weck *et al.* (2015). These conditions are fully satisfied. The generic necessary and sufficient Born criterion is that all eigenvalues of the C matrix be positive (Mouhat & Coudert, 2014). The C matrix was diagonalized numerically and all eigenvalues were found to be positive. As the above condition is satisfied, the mechanical stability of uranophane-α may be inferred.

The fact that $C33$, the diagonal component of the C matrix along c direction, is much smaller than either $C11$ or $C22$ suggests that thermal expansion of the material will occur predominantly perpendicular to the uranyl silicate sheets. This is consistent with the fact that the intersheet space, containing the hydrated Ca ions and free water molecules, will increase as temperature increases. The diagonal component $C11$ (a direction contained in the plane of the uranyl silicate sheets; see Fig. 1a) is the largest.

If single-crystal samples are not available, measurement of the individual elastic constants is not feasible. Instead, the polycrystalline bulk modulus (B) and shear

modulus (G) may be determined experimentally. The Voigt (1928) and Reuss (1929) schemes were used to compute the isotropic elastic properties of uranophane polycrystalline aggregates, as was done in our previous studies of rutherfordine and soddyite minerals (Colmenero *et al.*, 2017a,c). The Reuss and Voigt approximations result in lower and upper limits of polycrystalline constants, respectively, and practical estimates of the polycrystalline bulk and shear moduli in the Hill approximation may be computed by using average formulae (Hill, 1952). Relevant formulae for these approximations may be found in previous work (*e.g.* Bouhadda *et al.*, 2012; Weck *et al.*, 2015). The bulk and shear moduli and other mechanical properties computed in the Voigt, Reuss and Hill approximations are listed in Table 3.

The numerical estimate of the error in the computed bulk modulus given by the *CASTEP* code is 2.455 GPa, which is reasonable and very similar to the difference of the values in the Hill and Voigt/Reuss schemes of 2.721 GPa. Thus, the error was estimated to be ~5%. The Voigt and Reuss methods yield quite small differences for uranophane-α. Larger differences are expected for crystalline systems with strong anisotropy, featuring large differences between elastic constants along different directions (Weck *et al.*, 2015; Colmenero *et al.*, 2017a).

In general, a large value of the shear modulus is an indication of the more pronounced directional bonding between atoms (Ravindran *et al.*, 1998). The shear modulus, G, represents the resistance to plastic deformation, while the bulk modulus represents the resistance to fracture (Ravindran *et al.*, 1998; Bouhadda *et al.*, 2012). Young's modulus, B, defines the relationship between stress (force per unit area) and strain (proportional deformation) in a material; that is, $E = \sigma/\varepsilon$. It is possible to get the individual components of the bulk and Young's moduli from the elastic compliance matrix components (Ravindran *et al.*, 1998; Bouhadda *et al.* 2012; Weck *et al.*, 2015). The compliance matrix is the inverse of the stiffness C matrix. The corresponding values for the structure of uranophane are given in Table 4. B_c is much smaller than either B_a or B_b (Table 4). Thus, c direction is the most compressible one. Also, the component E_c is much smaller (less stiff) than E_a and E_b. Thus, the direction perpendicular to the plane containing the uranyl silicate sheets is the most compressible and the least stiff, which is in agreement with results for the elasticity C matrix.

Pugh (1954) introduced the proportion of bulk to shear moduli of polycrystalline phases ($D = B/G$) as a

TABLE 3. Bulk, modulus, shear modulus, Young modulus, Poisson ratio, Pugh's ratio and Vickers hardness (B, G, E, v, D and H) calculated in the Voigt, Reuss and Hill approximations. Values of B, G and E are given in GPa.

Property	Voigt	Reuss	Hill
B	61.9215	56.4799	59.2007
G	38.9723	34.0691	36.5207
E	96.6419	85.0969	90.8752
v	0.2399	0.2489	0.2442
D	1.5889	1.6578	1.6210
H	6.9163	5.7218	6.3253

TABLE 4. Bulk and Young moduli components (GPa) along the crystallographic axes.

Property	a axis	b axis	c axis
B	246.35	221.84	109.43
E	139.47	138.26	91.33

measure of ductility by considering the interpretation of the shear and bulk moduli given above. A larger D value is usually associated with greater ductility. The critical value that separates ductile and brittle materials is 1.75 (*i.e.* if $D > 1.75$, the material behaves in a ductile manner, otherwise the material behaves in a brittle manner; Bouhadda *et al.*, 2012). The Poisson ratio, v, can be also utilized to measure the malleability of crystalline compounds and is related to the Pugh's ratio given above by the relationship $D = (3 - 6v)/(8 + 2v)$. The Poisson ratio is ~0.33 (1/3) for ductile materials and much lower than 0.33 for brittle materials. The D and v values for uranophane are 1.62 and 0.24, respectively (Table 3). These values are only slightly smaller than 1.75 and 0.33, respectively, corresponding to a brittle material. For comparison, both studtite and metastudtite minerals are ductile (Weck *et al.*, 2015).

The hardness of these systems is computed according to a recently introduced empirical scheme (Chen *et al.*, 2011; Niu *et al.*, 2011) that correlates the Vickers hardness and Pugh's ratio ($D = B/G$). The Vickers hardness value, H, of polycrystalline uranophane (~6.3) corresponds to material of intermediate hardness (Table 3). For comparison, we obtained the hardness of studtite and metastudtite using the elasticity data of Weck *et al.* (2015). These systems, characterized by much larger D ratios, have much

smaller hardnesses (<1). The hardness of uranophane is comparable to soddyite, a uranyl silicate mineral (6.3 according to Colmenero *et al.*, 2017c).

In order to assess the elastic anisotropy of uranophane, shear anisotropic factors were obtained. These factors provide a measure of the degree of anisotropy in the bonding between atoms in different planes and are very important to studying material durability (Ravindran *et al.*, 1998; Bouhadda *et al.*, 2012). Shear anisotropic factors for the {100} (A_1), {010} (A_2) and {001} (A_3) crystallographic planes and percentages of anisotropy in compression and shear (A_{comp} and A_{shear}) were computed using the formulae given by Ravindran *et al.* (1998). For an isotropic crystal, the factors A_1, A_2 and A_3 must be 1, while any value smaller or greater than unity is a measure of the degree of elastic anisotropy of the crystal. Also, a value of 0% for A_{comp} and A_{shear} represents a perfectly isotropic crystal. For uranophane (see Table 5), the anisotropies grow in the planes {100}, {010} and {001} in the order $A_1 < A_2 < A_3$. The {100} plane is shown to be the most anisotropic one. Percentage anisotropies in compression and shear are ∼5% and 7%, respectively.

In the recently introduced universal anisotropy index (Ranganathan & Ostoja-Starzewski, 2008), the departure of A^U from zero defines the extent of single-crystal anisotropy and accounts for both the shear and the bulk contributions, unlike all other existing anisotropy measures. Thus, A^U represents a universal measure to quantify the single-crystal elastic anisotropy. Uranophane is characterized by an anisotropy index of 0.81, which is a rather small value ($A^U = 0$ corresponds to a perfectly isotropic crystal). For comparison, studtite and metastudtite exhibit much larger anisotropies. The values computed by Weck *et al.* (2015) are 2.17 and 1.44, respectively. Uranophane and soddyite, uranyl silicate minerals, are characterized by small anisotropies, A^U, of 0.81 and 0.50 (Colmenero *et al.*, 2017c), respectively.

A set of fundamental physical properties may be estimated with the calculated elastic constants. For example, V_L and V_T, the longitudinal and transverse elastic wave velocities of the polycrystalline materials, may be determined in terms of the bulk and shear moduli (Weck *et al.*, 2015). The values obtained are 3.069 and 5.276 km/s, respectively, using the calculated crystal density of 3.877 g/cm³ (see Table 1).

Lattice volumes around the equilibrium were calculated by optimizing the structure at 17 different applied pressures between –1.0 and 12.0 GPa. The calculated volume and pressure data were then fitted to a fourth-order Birch–Murnaghan (Birch, 1947) equation of state (EOS):

$$P = 3\,B\,f_E\,(1 + 2f_E)^{\frac{5}{2}}\left[1 + \frac{3}{2}(B' - 4)f_E \right.$$
$$\left. + \frac{3}{2}\left\{B\,B'' + (B' - 4)(B' - 3) + \frac{35}{9}\right\}f_E^2\right]$$

by using the *EOSFIT 5.2* code (Angel, 2001). The computed volume of the unit cell at 0 GPa (733.6 Å³) was fixed as V_0. In this EOS,

$$f_E = \frac{1}{2}\left[\left(\frac{V_0}{V}\right)^{\frac{2}{3}} - 1\right]$$

and B, B' and B'' are the bulk modulus and its first and second derivatives, respectively, at the temperature of 0 K. The values found for B, B' and B'' were $B = 59.96$ (± 2.1), $B' = 2.29$ (± 1.11), and $B'' = -0.25$ (± 0.19) GPa ($\chi 2 = 0.014$). The value obtained for the bulk modulus is in good agreement with that determined from elastic constants. For comparison, the bulk modulus obtained in the Hill approximation is $B = 59.20 \pm 2.45$ GPa.

Raman spectra and band assignment

In this section, we analyse the theoretically determined Raman spectrum and compare the main band wavenumbers obtained with the corresponding values found experimentally in the literature for this mineral phase (Frost *et al*., 2006a,b). Additional information about the Raman spectrum of uranophane can be found in Amme *et al.* (2002), Wall *et al.* (2010), Driscoll *et al.* (2014) and Bonales *et al.* (2015). The experimental band wavenumbers of Frost *et al.* (2006a, b) and their assignments are given in Supplementary Table S2. Experimental and calculated Raman shifts, calculated intensities and assignments are listed in Table 6. For visual comparison, the spectrum computed at T = 298 K, λ = 532 nm, full width at half maximum (FWHM) = 20 cm⁻¹ is shown in Fig. 2, where it is compared with an experimental spectrum from the RRUFF database (Downs, 2006; record RRUFF-050380). The two spectra are very similar to each other (Fig. 2). Pictures of the atomic motions in some of the Raman-active vibrational modes are given in Supplementary Fig. S3.

Although the bands in the OH stretching region seem to vary among samples, most bands are well reproduced theoretically. The wavenumbers of these bands observed in the experimental samples are

TABLE 5. Shear anisotropy factors (A_1, A_2 and A_3), percentages of anisotropy in compression and shear (A_{comp} and A_{shear}) and universal anisotropy index (A^U).

A_1	A_2	A_3	A_{comp} (%)	A_{shear} (%)	A^U
0.4448	0.5094	0.6301	4.5959	6.7129	0.8159

generally comparable but not identical (Frost *et al*., 2006a,b). This supports the presence of mobile protons that may be exchanged between the uranyl silicate sheets and the interlayer and that influence the hydrogen-bonding networks in their crystal structures (Cejka *et al.*, 1999; Frost *et al*., 2006b). The experimental bands centred at ~3492, 3463, 3358, 3326, 3310, 3216 and 3142 cm^{-1} are comparable with the calculated wavenumbers of 3485, 3478, 3357, 3295, 3272, 3238 and 3149 cm^{-1}. The theoretical methods allow us to distinguish the origins of these bands, which may be assigned to specific stretching vibrations. The first two modes (3492 and 3463 cm^{-1}) are attributed to stretching vibrations of structural OH (labelled as *cr* in Table 6). The next three bands (3358, 3326 and 3310 cm^{-1}) are due to vibrations localized on structural (coordinated) water molecules (labelled as *st* in Table 6). The band at 3216 cm^{-1} is ascribed to vibrations in crystallization and structural water molecules and OH stretching vibrations in SiO_3OH fragments, including OH groups that do not form part of the Ca atom coordination sphere (referred to as *fr* in Table 6). Finally, the band at 3142 cm^{-1} is assigned to vibrations in structural water molecules and SiO_3OH fragments including OH groups, which are not coordinated with interlayer Ca atoms. In previous experimental works, all of these bands were attributed without specification to OH stretching vibrations in the water molecules. The bands at lower wavenumbers also contain contributions from OH stretching vibrations from the free SiO_3OH fragments. Frost *et al.* (2006a) placed these vibrations at wavenumbers higher than 3600 cm^{-1}. However, in another study (see Frost *et al.*, 2006b), these vibrations were placed at about 3200 cm^{-1}.

The water bending vibration is not observed in the experimental Raman spectra and, accordingly, the corresponding computed band at 1639 cm^{-1} has a very small intensity (see vibrational mode picture in Fig. S3).

The experimental bands located at 1272 and 1156 cm^{-1} are placed at 1222 and 1146 cm^{-1} in the computed spectrum. These are assigned, respectively, to SiOH bending vibrations localized in the SiO_3OH fragments, whose OH groups are coordinated with interlayer Ca atoms (referred to as *co* in Table 6), and to free SiO_3OH fragments (referred to as *fr* in Table 6, as has already been mentioned).

The experimental bands at 960 and 950 cm^{-1} are close to the theoretical ones located at wavenumbers 958 and 942 cm^{-1}, respectively. Both bands are ascribed to SiOH bending vibrations localized in the *co*-SiO_3OH fragments, δ(*co*-SiOH), combined with water librations. These bands were, however, assigned to silicate stretching vibrations, $\nu^s(SiO_4^{4-})$ (ν_1), in most experimental works (Amme *et al.*, 2002; Frost *et al.*, 2006a,b; Wall *et al.*, 2010; Driscoll *et al.*, 2014; Bonales *et al.*, 2015). This assignment seems, therefore, not to be correct. It should also be noted that the correspondence with symmetric vibrations of the free silicate group are lost for uranophane (monoclinic symmetry), as can be seen in the vibrational mode pictures (Fig. S3). The contribution of SiO_3OH group vibrations to these modes is very small. A band appears in the calculated spectrum at 915 cm^{-1}, which is assigned to SiO stretching vibrations of the SiO_3OH fragments with coordinated OH groups (see vibrational mode picture in Fig. S3). Thus, silicate stretching vibrations appear at smaller wavenumbers than those reported in the experimental works (Frost *et al.*, 2006a; Wall *et al.*, 2010; Driscoll *et al.*, 2014).

The band placed at 886 cm^{-1} is obtained theoretically at 884 cm^{-1}, and that at 839 cm^{-1} is calculated to be at 837 cm^{-1}. Both bands are assigned to SiOH bending vibrations (localized in *fr*- and *co*-SiO_3OH fragments) and water librations.

The band placed at 797 cm^{-1} is the most intense of the Raman spectrum and it is calculated to be at 776 cm^{-1}. This band has been assigned in the experimental studies (Amme *et al.*, 2002; Frost *et al.*, 2006a,b; Wall *et al.*, 2010; Driscoll *et al.*, 2014; Bonales *et al.*, 2015) to symmetric uranyl stretching vibrations, $\nu^s(UO_2^{2+})$. However, our calculations show that it is the result of a combination of vibrations including SiOH vibrations localized in *fr*-SiO_3OH

TABLE 6. Experimental and calculated Raman band frequencies, calculated intensities and assignments. The irreducible representations (Irr. Rep.) corresponding to the ν vibrational motions associated with each band A or B are also given below.

| Experimental Raman shift (cm^{-1})	Calculated Raman shift (cm^{-1})	Irr. Rep. (C$_{2v}$)	Intensity (Å^4)	Assignment
3492[a]	3485	B	543.453	ν(OH) [cr-H$_2$O]
3463[a]	3478	A	234.841	
3358[a]	3359	B	206.215	ν(OH) [st-H$_2$O]
	3357	A	241.922	
3326[b]	3295	B	1298.612	
3310[b]	3272	B	1627.297	
3216[a]	3238	B	2003.074	ν(OH) [cr- and st-H$_2$O and fr-SiOH]
	3222	B	638.256	
3142[b]	3149	B	2468.104	ν(OH) [st-H$_2$O and fr-SiOH]
1272[b]	1222	B	22.349	δ(co-SiOH)
1169[b]	1146	B	13.621	δ(fr-SiOH)
964, 960[a]	958	B	102.979	δ(co-SiOH) + l(H$_2$O)
950[a]	942	B	126.692	
886[a]	884	B	25.099	δ(SiOH) + l(H$_2$O)
839[a]	857	A	23.425	δ(fr-SiOH) + l(H$_2$O)
	837	B	25.221	δ(SiOH) + l(H$_2$O)
	813	B	29.204	δ(SiOH) + l(H$_2$O) + ν(UO$_2$)
797, 793[a]	804	B	113.942	δ(SiOH) + l(H$_2$O) + ν(UO$_2$)
	776	B	767.503	δ(fr-SiOH) + l(H$_2$O) + ν(UO$_2$)
786[a]	766	B	504.625	δ(fr-SiOH) + l(H$_2$O) + ν(UO$_2$)
	760	B	521.123	
711[a]	717	B	103.711	δ(fr-SiOH) + l(H$_2$O)
	686	B	104.691	
627[b]	618	B	72.848	δ(co-SiOH) + l(H$_2$O)
545[a]	539	B	8.337	l(H$_2$O)
525[b]	524	B	9.467	δ(co-SiO$_3$OH) + l(H$_2$O)
	519	B	15.642	δ(fr-SiO$_3$OH) + l(H$_2$O)
469[a]	459	B	21.980	δ(co-SiO$_3$OH) + l(H$_2$O)
	452	B	48.164	δ(fr-SiO$_3$OH) + l(H$_2$O)
444[b]	434	B	29.965	δ(co-SiO$_3$OH) + l(H$_2$O)
399[a]	399	B	61.655	δ(co-SiO$_3$OH) + l(H$_2$O)
376[a]	374	B	44.165	δ(fr-SiO$_3$OH) + δ(UO$_2$) + l(H$_2$O)
347[a]	333	A	11.578	δ(fr-SiO$_3$OH) + δ(UO$_2$) + l(H$_2$O)
325[a]	317	B	12.801	δ(SiO$_3$OH) + δ(UO$_2$) + l(H$_2$O)
306[a]	316	A	23.824	δ(co-SiO$_3$OH) + δ(UO$_2$) + l(H$_2$O)
289[a]	289	A	18.128	δ(co-SiO$_3$OH) + δ(UO$_2$) + l(H$_2$O)
	288	B	9.997	δ(SiO$_3$OH) + δ(UO$_2$) + l(H$_2$O)
280[a]	276	A	11.180	δ(fr-SiO$_3$OH) + δ(UO$_2$) + l(H$_2$O)
250[a]	256	B	13.132	δ(SiO$_3$OH) + δ(UO$_2$) + l(H$_2$O)
214[a]	226	A	17.045	δ(SiO$_3$OH) + δ(UO$_2$) + l(H$_2$O)
205[a]	206	B	18.514	δ(SiO$_3$OH) + δ(UO$_2$) + l(H$_2$O)
167[a]	186	A	4.163	δ(SiO$_3$OH) + δ(UO$_2$) + l(H$_2$O)
	175	B	3.374	δ(SiO$_3$OH) + δ(UO$_2$) + l(H$_2$O)
139[a]	138	B	4.891	δ(co-SiO$_3$OH) + δ(UO$_2$) + l(H$_2$O)
137[a]	135	A	1.229	δ(co-SiOH) + l(H$_2$O)
122[a]	126	B	7.777	δ(SiO$_3$OH) + δ(UO$_2$) + l(H$_2$O)
112[a]	119	B	4.741	δ(SiO$_3$OH) + δ(UO$_2$) + l(H$_2$O)

[a] Frost *et al.* (2006a). [b] Frost *et al.* (2006b).
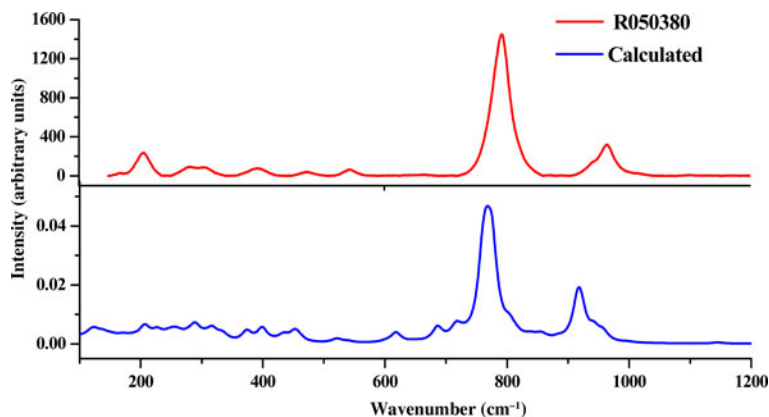
FIG. 2. Raman spectra of uranophane-α mineral. Red = RRUFF-050380 [82]; blue = calculated.

fragments, uranyl stretching vibrations and water librations. The uranyl vibrations make only a small contribution to this mode. As has already been mentioned, the symmetry of this vibration is lost and, therefore, the term 'symmetric' should not be used. A weak band at 786 cm^{-1} is also observed and it is comparable to calculated bands at 760 and 766 cm^{-1} having the same assignment with the intense band at 798 cm^{-1}.

For the bands at 711, 627, 544, 525, 469, 444 and 399 cm^{-1}, we obtain the theoretical counterparts 717, 618, 539, 519, 452, 434 and 399 cm^{-1}, which correspond to different *fr-* and *co*-SiOH bending vibrations. The band placed at 544 cm^{-1}, and found at 539 cm^{-1}, is attributed only to water librational vibrations.

Uranyl bending vibrations begin to appear at about 376 cm^{-1}. Bands at 376, 347, 325, 306, 289, 280, 250, 214, 205, 167, 139, 137, 122 and 112 cm^{-1} are close to their calculated counterparts at 374, 333, 317, 316, 289, 276, 256, 226, 206, 186, 137, 135, 126 and 119 cm^{-1}. Most of them are assigned to a combination of silicate, SiO$_3$OH, deformations (localized in *fr* or *co* groups), uranyl bending vibrations and water librations. The bands in this region have been assigned to uranyl bending vibrations (Frost *et al.*, 2006a). However, uranyl bending vibration has only a generally small contribution to these modes and is accompanied by silicate deformation vibrations and water librations. The precise assignments are given in Table 6.

Band assignment is a very difficult task in the case of complex systems with low symmetry. While the assignments made by correlating the bands with those of free fragments (Nakamoto, 1986; Cejka, 1999) are generally very useful for understanding the origins of the experimental bands, correspondence cannot always be made, especially for many systems with low symmetry (monoclinic for uranophane). For example, as is shown here, vibrations with specific motions similar to those of free silicate fragments (as v_3[SiO$_4^{4-}$], v_1[SiO$_4^{4-}$], v_4[SiO$_4^{4-}$] and v_2[SiO$_4^{4-}$]) and free uranyl fragments (v_3[UO$_2^{2+}$], v_1[UO$_2^{2+}$] and v_2[UO$_2^{2+}$]) were not observed for uranophane-α.

Sr-exchanged uranophane-α

The possible incorporation of strontium within the structure of uranophane-α was investigated by Douglas *et al.* (2002). This research was conducted in order to analyse whether this 1:1 uranyl silicate might serve as a host for the incorporation of fission products by substitution of Ca^{2+} in the interlayer space. Uranophane-α was synthesized by those authors and Ca^{2+} was exchanged completely or partially. The resulting solid was then characterized by XRD, SEM and elemental analysis. The Sr^{2+} analogue of uranophane yielded a diffractogram that resembles the XRD pattern obtained for synthetic uranophane, although the morphology of the solid was different.

Theoretical methods allow us to study this incorporation in a simple way that is free of the difficulties related to the radiotoxicity of these materials. We have studied the Sr-exchanged uranophane material by replacing the Ca^{2+} ion with Sr^{2+} in the structure of uranophane and performing a structural re-optimization under the same theoretical conditions as for ordinary Ca-uranophane (Table 7). The crystal

TABLE 7. Calculated lattice parameters of normal and Sr-exchanged uranophane-α.

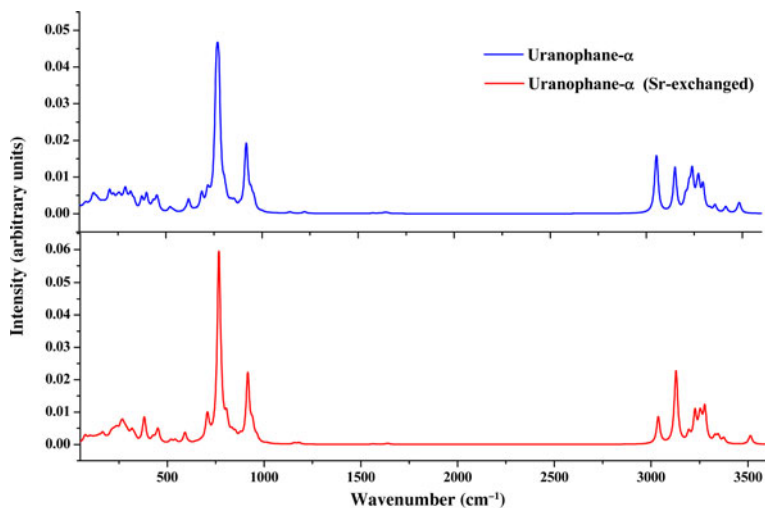| Parameter	a (Å)	b (Å)	c (Å)	α	β	γ	Volume (Å^3)	Density (g/cm^3)
Ca-uranophane-α	6.6689	7.0022	15.8684	90.0	98.0748	90.0	733.65	3.877
Sr-uranophane-α	6.6959	7.0233	16.2127	90.0	97.3650	90.0	756.15	3.970

FIG. 3. Computed Raman spectra of Ca- and Sr-exchanged uranophanes.

structure demonstrated very small variations upon exchange. The interlayer cation solvation sphere was very similar to that of Ca-uranophane. The same structure was obtained when the calculations were made from different initial forms of the hydrogen bond structure in the interlayer space. The corresponding lattice parameters are given in Table 7. The main difference is the increase in the interlayer space, corresponding to an increase of 0.35 Å in the c lattice parameter. The change of a and b lattice parameters was only of about 0.02 Å. The volume is increased by ~3%. These results may be compared with those of Berghout *et al.* (2010) for the Ca- and Sr-exchanged two-layer hydrate smectites. In this case, the computed increase in the c lattice parameter was ~0.21 Å and the unit-cell volume increased by 2.4%.

The XRD traces of Ca- and Sr-exchanged uranophanes were obtained from the optimized atomistic positions using the program *REFLEX* included in the Materials Studio package (Materials Studio, 2018). As expected from the study of Douglas *et al.* (2002), the XRD traces of both forms are very similar (see Fig. S2).

In order to detect whether these materials might be distinguished by Raman spectroscopy, we computed the corresponding spectra of Sr-exchanged uranophane using density functional perturbation theory. The corresponding spectra were again very similar (Fig. 3).

As the motion of the interlayer cation does not appear in any of the main bands in the Raman spectrum (see vibrational mode pictures in Fig. S3) and the solvation structure of the interlayer cation remains almost unchanged, the Raman spectra of Ca- and Sr-exchanged uranophanes are very similar. In summary, the incorporation of Sr^{2+} in the structure of uranophane by cation exchange is possible, in accordance with the experimental results of Douglas *et al.* (2002), and the identification of the exchanged solid is not feasible either by XRD or by Raman spectroscopy.

SUMMARY AND CONCLUSIONS

The DFT results show the important role of water in the structural and vibrational properties of the uranyl silicate mineral, uranophane-α. Water molecules enter into the structure of uranophane-α as structural and interlayer water not bound to interlayer cations. Structural water molecules form part of the coordination structure of calcium ions present in the interlayer space between the uranyl silicate sheets, *i.e.* within the distorted pentagonal bipyramids, $CaO_2(OH)(H_2O)_4$. Such interlayer water molecules are also localized in the interlayer space, but are free (*i.e.* they do not coordinate the calcium ions). Structural optimization performed by the GGA-PBE exchange-correlation functional, taking into account a dispersion correction scheme, has produced unit-cell lattice parameters and atomic-bond distances in excellent agreement with experimental data. The computed XRD pattern is also in very good agreement with the experimental one.

An analysis of the calculated elasticity stiffness tensor has revealed that the uranophane-α structure satisfies properly the mechanical stability conditions. Furthermore, the mechanical properties of this mineral, for which there are no experimental data to compare with, were predicted. Uranophane-α is a brittle material characterized by small anisotropy and large hardness in comparison with those of other uranyl-containing materials. The EOS of uranophane-α was obtained by fitting lattice volumes and pressures to a fourth-order Birch–Murnaghan EOS.

The Raman spectrum was also computed by means of density functional perturbation theory and compared with its experimental counterpart. The results were in good agreement with the experimental data. A normal mode analysis of the theoretical spectrum was carried out and used to assign the main bands of the Raman spectra. Theoretical methods allowed the assignment of the bands to vibrations localized in different fragments within the crystal unit cell.

The main bands used as fingerprints to identify uranophane-α are those placed at wavenumbers 797 and 960 cm^{-1}. The corresponding values resulting from our computations are comparable to the experimental values of 776 and 958 cm^{-1}. The first band is assigned to a combination of SiOH bending vibrations localized in the *fr*-SiO_3OH fragments, uranyl UO stretching vibrations and water librations. The second one is assigned to a combination of SiOH bending vibrations localized in the *co*-SiO_3OH fragments and water librations. In the experimental works, these bands were attributed to uranyl symmetric stretching,

$v^s(UO_2^{2+})$, and silicate symmetric stretching, $v^s(SiO_4^{4-})$, vibrations. As indicated by our theoretical calculations, these assignments are incorrect or incomplete since they do not include several contributions, such as those coming from vibrations arising from the ubiquitous water molecules and SiOH fragments. These contributions underline the role of the hydrogen bond structure in uranophane-α and its impact on the vibrational spectra. Furthermore, the correlation of these bands with those of free fragments is lost due to the low crystal symmetry.

The bands at 545, 469 and 399 cm^{-1} were also satisfactorily reproduced theoretically, with the corresponding values being 539, 459 and 399 cm^{-1}. The first band is only ascribed to water librational vibrations, and the remaining ones represent SiOH bending vibrations localized in the *co*-SiO_3OH fragments and water librational vibrations. Previous assignments of these bands are not correct since they involve silicate group deformations, $v_4(SiO_4^{4-})$ and $v_2(SiO_4^{4-})$. In addition, testing for the correspondence with free silicate group vibrations cannot be performed for uranophane.

In the low-wavenumber region, there are four main bands located at 289, 250, 205 and 167 cm^{-1}, which were determined theoretically to be placed at 289, 256, 206 and 186 cm^{-1}, respectively. These were mainly attributed to uranyl bending vibrations. Theoretical calculations indicate that these bands correspond to a combination of silicate (SiO_3OH) deformations, uranyl bending vibrations and water librations. The uranyl bending vibration appears to make only a small contribution.

In the OH stretching region, most bands were well reproduced theoretically, in spite of the fact that the bands in this region vary among samples. The theoretical analysis allowed for the assignment of these bands to vibrations localized in different fragments of the unit cell. The bands at higher wavenumbers are attributed to OH stretching vibrations in crystallization water molecules. The bands at medium wavenumbers are due to OH stretching vibrations localized in structural water molecules. Finally, the bands with the lowest wavenumbers contain contributions from OH stretching vibrations localized in the SiOH fragments containing OH groups out of the coordination sphere of interlayer calcium ions.

The bands placed at 1272 and 1156 cm^{-1} (comparable to the theoretical bands located at 1222 and 1146 cm^{-1}, respectively) are attributable to SiOH bending vibrations, localized in different SiO_3OH

fragments (the higher wavenumber bands in *co*-SiO₃OH fragments and the lower wavenumber bands in *fr*-SiO₃OH fragments).

Finally, the structure of Sr-exchanged uranophane and the structure of the solvation sphere of the interlayer cation are very similar to that of normal uranophane, the main difference being, as in the case of a smectite clay mineral (Berghout *et al.*, 2010), the increase of the interlayer space (the *c* parameter increased by about 0.35 Å). The XRD pattern and Raman spectrum of the Sr-exchanged uranophane were also almost identical to those of the normal Ca-uranophane, which is in agreement with the experimental results of Douglas *et al.* (2002).

SUPPLEMENTARY INFORMATION

Supplementary data associated with this article are given in a separate file (Supplementary Information). The first section of the Supplementary Information contains the details about the XRD powder patterns of uranophane-α. In this section, Fig. S1 shows the corresponding computed and experimental X-ray powder patterns and Table S1 gives the values of the positions and intensities of the main reflections. The second section shows a comparison of the computed X-ray powder patterns of Ca- and Sr-exchanged uranophanes (Fig. S2). Finally, the last section contains some details of the Raman spectra of this material. Namely, Table S2 gives a comparison of experimental Raman shifts of uranophane-α taken from several sources, and Fig. S3 provides graphical pictures of the Raman normal modes of uranophane-α.

The supplementary material for this article can be found at https://doi.org/10.1180/clm.2018.27.

REFERENCES

Amme M., Renker B., Schmid B., Feth M.P., Bertagnolli H. & Döbelin W. (2002) Raman microspectrometric identification of corrosion products formed on UO₂ nuclear fuel during leaching experiments. *Journal of Nuclear Materials*, **306**, 202–212.

Angel R.J. (2001) Equations of state. Pp. 35–60 in: *High-Temperature and High-Pressure Crystal Chemistry* (R.M. Hazen & R.T. Downs, editors). Reviews in Mineralogy and Geochemistry, **41**. Mineralogical Society of America, Chantilly, VA, USA.

Atencio D., Carvalho F.M.S. & Matioli P.A. (2004) Coutinhoite, a new thorium uranyl silicate hydrate, from Urucum mine, Galiléia, Minas Gerais, Brazil. *American Mineralogist*, **89**, 721–724.

Berghout A., Tunega D. & Zaoui A. (2010) Density functional theory (DFT) study of the hydration steps of Na⁺/Mg²⁺/Ca²⁺/Sr²⁺/Ba²⁺-exchanged montmorillonites. *Clays and Clay Minerals*, **58**, 174–187.

Birch F. (1947) Finite elastic strain of cubic crystal. *Physical Review*, **71**, 809–824.

Bonales L.J., Colmenero F., Cobos J. & Timón V. (2016) Spectroscopic Raman characterization of rutherfordine: a combined DFT and experimental study. *Physical Chemistry Chemical Physics*, **18**, 6575–6584.

Bonales L.J., Menor-Salván C. & Cobos J. (2015) Study of the alteration products of a natural uraninite by Raman spectroscopy. *Journal of Nuclear Materials*, **462**, 296–303.

Bouhadda Y., Djella S., Bououdina M., Fenineche N. & Boudouma Y. (2012) Structural and elastic properties of LiBH₄ for hydrogen storage applications. *Journal of Alloys and Compounds*, **534**, 20–24.

Burns P.C. (1998) The structure of boltwoodite and implications of solid solution toward sodium boltwoodite. *The Canadian Mineralogist*, **36**, 1069–1075.

Burns P.C. (1999a) The crystal chemistry of uranium. Pp. 23–90 in: *Uranium: Mineralogy, Geochemistry, and the Environment* (P.C. Burns & R. Finch, editors). Reviews in Mineralogy and Geochemistry, **38**. Mineralogical Society of America, Chantilly, VA, USA.

Burns P.C. (1999b) Cs boltwoodite obtained by ion exchange from single crystals: implications for radionuclide release in a nuclear repository. *Journal of Nuclear Materials*, **265**, 218–223.

Burns. P.C. (2001) A new uranyl silicate sheet in the structure of haiweeite and comparison to other uranyl silicates. *The Canadian Mineralogist*, **39**, 1153–1160.

Burns P.C. (2005) U⁶⁺ minerals and inorganic compounds: insights into an expanded structural hierarchy of crystal structures. *The Canadian Mineralogist*, **43**, 1839–1894.

Burns P.C. & Hill F.C. (2000) A new uranyl sheet in K₅[(UO₂)₁₀O₈(OH)₉](H₂O): new insight into sheet anion-topologies. *The Canadian Mineralogist*, **38**, 163–173.

Burns P.C. & Klingensmith A.L. (2006) Uranium mineralogy and neptunium mobility. *Elements*, **2**, 351–356.

Burns P.C. & Li Y. (2002) The structures of becquerelite and Sr-exchanged becquerelite. *American Mineralogist*, **87**, 550–557.

Burns P.C., Miller M.L. & Ewing R.C. (1996) U^{6+} minerals and inorganic phases: a comparison and hierarchy of crystal structures. *The Canadian Mineralogist*, **34**, 845–880.

Burns P.C., Ewing R.C. & Hawthorne F.C. (1997a) The crystal chemistry of hexavalent uranium; polyhedron geometries, bond-valence parameters, and polymerization of polyhedra. *The Canadian Mineralogist*, **35**, 1551–1570.

Burns P.C., Ewing R.C. & Miller M.L. (1997b) Incorporation mechanisms of actinide elements into the structures of U^{6+} phases formed during the oxidation of spent nuclear fuel. *Journal of Nuclear Materials*, **245**, 1–9.

Burns P.C., Deely K.M. & Skanthakumar S. (2004) Neptunium incorporation into uranyl compounds that form as alteration products of spent nuclear fuel: implications for geologic repository performance. *Radiochimica Acta*, **92**, 151–159.

Cejka J. (1999) Infrared spectroscopy and thermal analysis of the uranyl minerals. Pp. 521–622 in: *Uranium: Mineralogy, Geochemistry, and the Environment* (P.C. Burns & R. Finch, editors). Reviews in Mineralogy and Geochemistry, **38**. Mineralogical Society of America, Chantilly, VA, USA.

Clark S.J., Segall M.D., Pickard C.J., Hasnip P.J., Probert M.I.J., Refson K. & Payne M.C. (2005) First principles methods using CASTEP. *Zeitschrift für Kristallographie*, **220**, 567–570.

Colmenero F., Bonales L.J., Cobos J. & Timón V. (2017a) Thermodynamic and mechanical properties of the rutherfordine mineral based on density functional theory. *Journal of Physical Chemistry C*, **121**, 5994–6001.

Colmenero F., Bonales L.J., Cobos J. & Timón V. (2017b) Study of the thermal stability of studtite by *in situ* Raman spectroscopy and DFT calculations. *Spectrochimica Acta A*, **174**, 245–253.

Colmenero F., Bonales L.J., Cobos J. & Timón V. (2017c) Structural, mechanical and vibrational study of uranyl silicate mineral soddyite by DFT calculations. *Journal of Solid State Chemistry*, **253**, 249–257.

Colmenero F., Bonales L.J., Cobos J. & Timón V. (2017d) Density functional theory study of the structural, vibrational and thermodynamic properties of γ-UO$_3$ polymorph. *Journal of Physical Chemistry C*, **121**, 14507–14516.

Colmenero F., Fernández A. M., Cobos J. & Timón V. (2018a) Thermodynamic properties of uranyl containing materials based on density functional theory. *Journal of Physical Chemistry C*, **122**, 5254–5267.

Colmenero F., Fernández A. M., Cobos J. & Timón V. (2018b) Temperature dependent free energies of reaction of uranyl containing materials based on density functional theory. *Journal of Physical Chemistry C*, **122**, 5268–5279.

Chen X.-Q., Niu H., Li D. & Li Y. (2011) Modeling hardness of polycrystalline materials and bulk metallic glasses. *Intermetallics*, **19**, 1275–1281.

Demartin F., Gramaccioli C.M. & Pilati T. (1992) The importance of accurate crystal structure determination of uranium minerals. II. Soddyite $(UO_2)_2(SiO_4)\cdot$2H$_2$O. *Acta Crystallographica C*, **48**, 1–4.

Douglas M., Clark S.B., Utsunomiya S. & Ewing R.C. (2002) Cesium and strontium incorporation into uranophane, Ca[(UO$_2$)(SiO$_3$OH)]$_2$·5H$_2$O. *Journal of Nuclear Science and Technology*, **3**, 504–507.

Douglas M., Clark S.B., Friese J.I., Arey B.W., Buck E.C., Hanson B.D., Utsunomiya S. & Ewing R.C. (2005) Microscale characterization of uranium(VI) silicate solids and associated neptunium (V). *Radiochimica Acta*, **93**, 265–272.

Downs R.T., Bartelmehs K.L., Gibbs G.V. & Boisen M.B. (1993) Interactive software for calculating and displaying X-ray or neutron powder diffractometer patterns of crystalline materials. *American Mineralogist*, **78**, 1104–1107.

Downs R.T. (2006) The RRUFF Project: an integrated study of the chemistry, crystallography, Raman and infrared spectroscopy of minerals, Program and Abstracts of the 19th General Meeting of the International Mineralogical Association in Kobe, Japan, 2006. O03-13. Record RRUFF-050380 corresponds to a natural mineral sample from Grafton County, New Hampshire, USA. RRUFF database, URL http://rruff.info/uranophane.

Driscoll R.J.P., Wolverson D., Mitchels J.M., Skelton J. M., Parker S.C., Molinari M., Khan I., Geeson D. & Allen G.C. (2014) A Raman spectroscopic study of uranyl minerals from Cornwall, UK. *RSC Advances*, **4**, 59137–59149.

Finch R.J. & Ewing R.C. (1992) The corrosion of uraninite under oxidizing conditions. *Journal of Nuclear Materials*, **190**, 133–156.

Forbes T.Z. & Burns P.C. (2006) Ba(NpO$_2$)(PO$_4$)(H$_2$O), its relationship to the uranophane group, and implications for Np incorporation in uranyl minerals. *American Mineralogist*, **91**, 1089–1093.

Frondel C. (1956) Mineral composition of gummite. *American Mineralogist*, **41**, 539–568.

Frost R.L., Cejka J., Weier M.L. & Martens W.N. (2006a) Molecular structure of the uranyl silicates – a Raman spectroscopic study. *Journal of Raman Spectroscopy*, **37**, 538–551.

Frost R.L., Cejka J., Weier M.L. & Martens W.N. (2006b) Raman spectroscopy study of selected uranophanes. *Journal of Molecular Structure*, **788**, 115–125.

Ginderow D. (1988) Structure de l'uranophane alpha, Ca (UO$_2$)$_2$(SiO$_3$OH)$_2$.5H$_2$O. *Acta Crystallographica*, **44**, 421–424.

Grenthe I., Drozdzynski J., Fujino T., Buck E.C., Albrecht-Schmitt T.E. & Wolf S.F. (2006) Uranium. Pp. 253–638, in: *The Chemistry of the Actinide and Transactinide Elements, Vol. I* (L.R. Morss, N.M. Edelstein & J. Fuger, editors). Springer Science and Business Media, Berlin.

Grimme S. (2006) Semiempirical GGA-type density functional constructed with a long-range dispersion correction. *Journal Computational Chemistry*, **27**, 1787–1799.

Hill R. (1952) The elastic behaviour of a crystalline aggregate. *Proceedings of the Physical Society of London*, **65**, 349–354.

Huang J., Wang X. & Jacobson A.J. (2003) Hydrothermal synthesis and structures of the new open-framework uranyl silicates $Rb_4(UO_2)_2(Si_8O_{20})$ (USH-2Rb), $Rb_2(UO_2)_2(Si_2O_6)\cdot H_2O$ (USH-4Rb) and $A_2(UO_2)(Si_2O_6)\cdot 0.5H_2O$ (USH-5A, A = Rb,Cs). *Journal of Materials Chemistry*, **13**, 191–196.

Jackson J.M. & Burns P.C. (2001) A re-evaluation of the structure of weeksite, a uranyl silicate framework mineral. *The Canadian Mineralogist*, **39**, 187–195.

Jin G.B., Skanthakumar S. & Soderholm L. (2011) Two new neptunyl(V) selenites: a novel cation–cation interaction framework in $(NpO_2)_3(OH)(SeO_3)(H_2O)_2\cdot H_2O$ and a uranophane-type sheet in $Na(NpO_2)(SeO_3)(H_2O)$. *Inorganic Chemistry*, **50**, 6297–6303.

Jouffret L., Rivenet M. & Abraham F. (2010a) U(VI) oxygen polyhedra as pillars for building frameworks from uranophane-type layers. *IOP Conference Series: Materials Science and Engineering*, **9**, 012028.

Jouffret L.Rivenet M. & Abraham F. (2010b) A new series of pillared uranyl-vanadates based on uranophane-type sheets in the uranium-vanadium-linear alkyl diamine systems. *Journal of Solid State Chemistry*, **183**, 84–92.

Jouffret L., Shao Z., Rivenet M. & Abraham F. (2010c) New three-dimensional inorganic frameworks based on the uranophane-type sheet in monoamine templated uranyl-vanadates. *Journal of Solid State Chemistry*, **183**, 2290–2297

Klingensmith A.L. & Burns P.C. (2007) Neptunium substitution in synthetic uranophane and soddyite. *American Mineralogist*, **92**, 1946–1951.

Kuta J., Wang Z., Wisuri K., Wander M.C.F., Wall N.A. & Clark A.E. (2013) The surface structure of α-uranophane and its interaction with Eu(III) – an integrated computational and fluorescence spectroscopy study. *Geochimica et Cosmochimica Acta*, **103**, 184–196.

Materials Studio (2018) BIONIA Materials Studio Package http://accelrys.com/products/collaborative-science/biovia-materials-studio/

Mer A., Obbade S., Rivenet M., Renard C. & Abraham F. (2012) $[La(UO_2)V_2O_7][(UO_2)(VO_4)]$ the first lanthanum uranyl-vanadate with structure built from

two types of sheets based upon the uranophane anion-topology. *Journal of Solid State Chemistry*, **185**, 180–186.

Mouhat F. & Coudert F.-X. (2014) Necessary and sufficient elastic stability conditions in various crystal systems. *Physical Review B*, **90**, 224104.

Murphy W.M. & Grambow B. (2008) Thermodynamic interpretation of neptunium coprecipitation in uranophane for application to the Yucca Mountain Repository. *Radiochimica Acta*, **96**, 563–567.

Nakamoto K. (1986) *Infrared and Raman Spectra of Inorganic and Coordination Compounds*. J. Wiley and Sons, New York.

Niu H., Wei P., Sun Y., Chen X.-Q., Franchini C., Li D. & Li Y. (2011) Electronic, optical, and mechanical properties of superhard cold-compressed phases of carbon. *Applied Physics Letters*, **99**, 031901.

Novacek R. (1935) Study of some secondary uranium minerals. *Věstník Královské České Společnosti Nauk II*, **7**, 36.

Nye J.F. (1985) *The Physical Properties of Crystals: Their Representation by Tensors and Matrices*. Oxford University Press, New York.

Pearcy E.C., Prikryl J.D., Murphy W.M. & Leslie B. W. (1994) Alteration of uraninite from the Nopal I deposit, Peña Blanca District, Chihuahua, Mexico, compared to degradation of spent nuclear fuel in the proposed U.S. high-level nuclear waste repository at Yucca Mountain, Nevada. *Applied Geochemistry*, **9**, 713–732.

Perdew J.P., Burke K. & Ernzerhof M. (1996) Generalized gradient approximation made simple. *Physical Review Letters*, **77**, 3865–3868.

Plasil J. (2014) Oxidation-hydration weathering of uraninite: the current state-of-knowledge. *Journal of Geosciences*, **59**, 99–114.

Pugh S.F. (1954) XCII. Relations between the elastic moduli and the plastic properties of polycrystalline pure metals. *Philosophical Magazine*, **45**, 823–843.

Ranganathan S.L. & Ostoja-Starzewski M. (2008) Universal elastic anisotropy index. *Physical Review Letters*, **101**, 055504.

Ravindran P., Fast L., Korzhavyi P.A., Johansson B., Wills J. & Eriksson O. (1998) Density functional theory for calculation of elastic properties of orthorhombic crystals: application to $TiSi_2$. *Journal of Applied Physics*, **84**, 4891–4904.

Reuss A. (1929) Berechnung der Fliessgrenze von Mischkristallen auf Grund der Plastizitatsbedingung fur Einkristalle. *Zeitschrift für Angewandte Mathematik und Mechanik*, **9**, 49–58.

Shuller L.C., Ewing R.C. & Becker U. (2010) Quantum-mechanical evaluation of Np-incorporation into studtite. *American Mineralogist*, **95**, 1151–1160.

Shuller L.C., Ewing R.C. & Becker U. (2013) Np-incorporation into uranyl phases: a quantum-

mechanical evaluation. *Journal of Nuclear Materials*, **434**, 440–450.

Shuller L.C., Bender W.M., Walker S.M. & Becker U. (2014) Quantum-mechanical methods for quantifying incorporation of contaminants in proximal minerals. *Minerals*, **4**, 690–715.

Stohl F.V. & Smith D.K. (1981) The crystal chemistry of the uranyl silicate minerals. *American Mineralogist*, **66**, 610–624.

Troullier N. & Martins J.L. (1991) Efficient pseudopotentials for plane-wave calculations. *Physical Review B*, **43**, 1993–2006.

Tunega D., Bucko T. & Zaoui A. (2012) Assessment of ten DFT methods in predicting structures of sheet silicates: importance of dispersion corrections. *Journal of Chemical Physics*, **137**, 114105.

Viswanathan K. & Harneit O. (1986) Refined crystal structure of beta-uranophane, $Ca(UO_2)_2(SiO_3OH)_2 \cdot 5H_2O$. *American Mineralogist*, **71**, 1489–1493.

Voigt W. (1928) *Lehrbuch der Kristallphysik*. Teubner, Leipzig, Germany.

Wall N.A., Clark S.B. & McHale J.L. (2010) Synthesis and characterization of 1:1 layered uranyl silicate mineral phases. *Chemical Geology*, **274**, 149–157.

Weck P.F., Kim E. & Buck E.C. (2015) On the mechanical stability of uranyl peroxide hydrates: implications for nuclear fuel degradation. *RSC Advances*, **5**, 79090–79097.

Wheaton V., Majumdar D., Balasubramanian K., Chauffe L. & Allen P.G. (2003) A comparative theoretical study of uranyl silicate complexes. *Chemical Physics Letters*, **371**, 349–359.

Websky M. (1853) Über die geognostichen Verhaltnisse der Erzlagerstäten von Kupferberg u. Rudelstadt in Schlesien. *Zs. d. Deutsche Geologische Gesellschaft*, **V**, 391.

Websky M. (1859) Ueber Uranophan. *Zs. d. Deutsche Geologische Gesellschaft*, **XI**, 384.

Wronkiewicz D.J., Bates J.K., Gerding T.J., Veleckis E. & Tani B.S. (1992) Uranium release and secondary phase formation during unsaturated testing of UO_2 at 90°C. *Journal of Nuclear Materials*, **190**, 107–127.

Wronkiewicz D.J., Bates J.K., Gerding T.J., Veleckis E. & Tani B.S. (1996) Ten-year results from unsaturated drip tests with UO_2 at 90°C: implications for the corrosion of spent nuclear fuel. *Journal of Nuclear Materials*, **238**, 78–95.